ISSN (Print) 1226-1750
ISSN (Online) 2233-6656
Journal of Magnetics 31(3), 314-322 (2026) https://doi.org/10.4283/JMAG.2026.31.3.314

Magnetic Properties Analysis of Ultra-Thin Silicon Steel and Amorphous Alloy Ribbons Under Bending and Tensile Stresses

Yongjian Li[1]*, Xin Zhang[1], Shuaichao Yue[1], Haosen Sun[1], and Jian Huang[2]

[1]*State Key Laboratory of Intelligent Power Distribution Equipment and System, Hebei University of Technology, Tianjin 300401, China*
[2]*Tianjin Zhixin Electric Co., Ltd, Tianjin 300304, China*

(Received 16 March 2026, Received in final form 14 September 2026, Accepted 14 September 2026)

Ultra-thin silicon steel and amorphous alloy are commonly used materials in wound-core transformers, where the core is subjected to both bending and tensile stresses during manufacturing. To investigate the effect of stresses on the magnetic properties of these materials, this paper establishes a magnetic measurement system capable of applying synchronized bending and tensile forces. Using this system, magnetic properties of ultra-thin silicon steel and amorphous alloy strips are tested under bending-only and combined bending–tensile loading. Variations in hysteresis loops and core losses of both materials are analyzed. This study provides data and theoretical support for optimizing the core winding process and enhancing the performance of wound-core transformers.

Keywords : ultra-thin silicon steel, amorphous alloy, bending stress, tensile stress, magnetic properties

1. Introduction

Ultra-thin silicon steel and amorphous alloys are widely used in high-efficiency transformers and power electronic devices owing to their low core loss and high magnetic permeability [1, 2]. During slitting, winding, clamping, and assembly, these thin magnetic materials are subjected to externally applied and residual mechanical stresses. Through the inverse magnetostrictive effect, mechanical stress changes the magnetoelastic energy and effective magnetic anisotropy of a material, thereby modifying its magnetic-domain configuration and domain-wall motion. Consequently, permeability, coercivity, remanence, hysteresis loop shape, and core loss may substantially change under mechanical loading. The magnitude and direction of these changes depend on the magnetostriction coefficient, material texture, loading direction, stress level, and heat treatment state. In a wound structure, bending results in a non-uniform stress distribution across the ribbon thickness, while winding tension introduces additional axial tensile stress. Therefore, measurements from stress-free flat specimens cannot fully represent the magnetic behaviour of ribbons in practical wound cores.

©The Korean Magnetics Society. All rights reserved.
*Corresponding author: Tel: +8613802065108,
E-mail: 2002092@hebut.edu.cn

Recent studies on electrical steels have progressed from conventional planar uniaxial loading experiments towards measurements under directional, bending, and multi-physics loading conditions. Dou *et al.* investigated the effects of the uniaxial stress applied along different directions on the alternating magnetic properties of silicon steel sheets [3]. Maeda *et al.* developed an apparatus for characterizing electrical steel sheets under compressive stress normal to the sheet surface [4]. Daem *et al.* quantified decline in permeability and core loss caused by plastic deformation and residual stress in silicon steel [5]. Rękas *et al.* subsequently developed a yoke-based setup for measuring the magnetoelastic properties of electrical steels while considering the angle between the applied mechanical stress and magnetization direction [6]. For curved specimens, Chen *et al.* measured the hysteresis and loss properties of grain-oriented electrical steel under bending stress over a frequency range of 50–1000 Hz [7] and subsequently examined the combined effects of bending stress, temperature, and non-sinusoidal excitation [8]. These studies demonstrate that mechanical loading produces an anisotropic magnetic response and that bending or residual stress generally reduces permeability and increases core loss. They also show that the extent of magnetic deterioration depends on the stress state, excitation frequency, and magnetization waveform.

With respect to amorphous magnetic materials, Mizuta

© 2026 Journal of Magnetics

et al. compared the magnetic properties of individual amorphous ribbons and laminated specimens under tensile and compressive stresses [9]. Zhu *et al.* subsequently investigated the hysteresis loops and loss characteristics of laminated 1K101 amorphous sheets under tensile and compressive stresses from 50 Hz to 4 kHz demonstrating that the stress-dependent change in the total loss was primarily governed by the hysteresis loss component [10]. More recently, Li *et al.* combined macroscopic magnetic measurements with magneto-optical observations and related the stress-dependent magnetic behaviour of 1K101 amorphous ribbons to tensile–stress-induced magnetic anisotropy and magnetic-domain rearrangement [11]. Studies of amorphous wound cores have further demonstrated that core geometry, magnetic annealing, and winding-related mechanical conditions can considerably affect the measured magnetic characteristics and magneto-mechanical vibrations [12, 13]. Nevertheless, measurements performed on finished wound cores cannot generally distinguish the effects of bending curvature, winding tension, residual stress, core structure, and heat treatment independently.

Despite these advances, most previous investigations have considered flat specimens under uniaxial tensile or compressive loading, curved specimens under bending-only conditions, or finished-wound cores containing several coupled manufacturing effects. Conventional SST and Epstein-frame arrangements are designed primarily for standardized measurements of flat samples and cannot simultaneously reproduce controllable curvature and axial tension during ribbon winding. To address this issue, a testing system capable of exerting controllable tensile forces to ring ultra-thin silicon steel or amorphous alloy ribbon samples is designed and constructed. Utilizing an electric cylinder driven by a servo motor and an adjustable sample frame, the system can apply tensile stress up to 40 MPa and varying bending stresses by adjusting the curvature. The proposed system enables investigation of the individual and coupled effects of the bending and tensile stresses on hysteresis loops, coercivity, permeability and core loss under identical measurement conditions. GT050 ultra-thin grain-oriented silicon steel and 1K101 amorphous ribbon are directly compared at 50 Hz with the same curvature and tensile loading, providing experimentally consistent data for design and manufacturing optimization of wound magnetic cores

2. Measurement System

To investigate the coupling effects of the bending and tensile stresses on the magnetic properties of ultra-thin silicon steel and amorphous alloy ribbons, a tunable measurement system for magnetic properties under combined stress is designed and constructed. The system primarily comprises a ribbon sample, a PC equipped with LabVIEW software and a data acquisition (DAQ) card, a power amplifier, a current sensor, an electric cylinder driven by a servo motor, a force sensor and several clamping blocks, as illustrated in Fig. 1.

The LabVIEW controller integrated with the DAQ card generates excitation signals, which are amplified by the power amplifier and then applied to the excitation winding, thereby inducing a sinusoidal alternating magnetic field in samples. The DAQ card collects the current signal from the current sensor and voltage signal from the *B*-coil

sensor; subsequently, these signals are processed by the LabVIEW program to derive the magnetic flux density *B*, and magnetic field strength *H*. The frequency-domain feedback algorithm and waveform compensation method are employed to ensure a sinusoidal *B* waveform. The axial tensile stress is directly monitored by the force sensor.

The parameters of the ultra-thin silicon steel and amorphous alloy samples are listed in Table 1. To measure the magnetization characteristics of the samples, an excitation coil (*H*-coil) and an induction coil (*B*-coil) are arranged at the centre of the samples (non-clamped region) to ensure that measurement is conducted in a region with a uniform stress distribution. The magnetic flux density *B* and magnetic field strength *H* values can be derived using Eqs. (1) and (2), respectively. The core loss of the bent samples can be determined by Eq. (3).

$$B(t) = -\frac{1}{N_2 S}\int_0^t V_2(t)dt \tag{1}$$

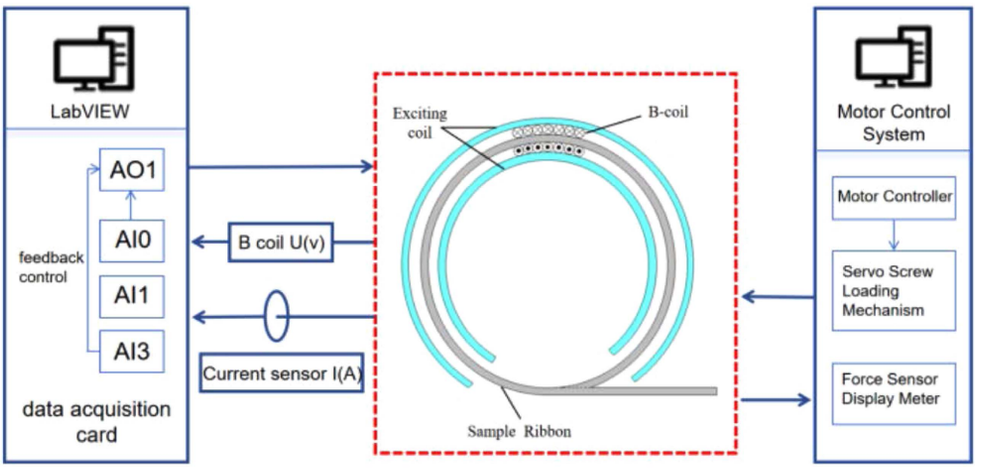
$$H(t) = \frac{N_1}{Le} I(t) \tag{2}$$

$$P_S = \frac{f}{\rho}\oint HdB \tag{3}$$

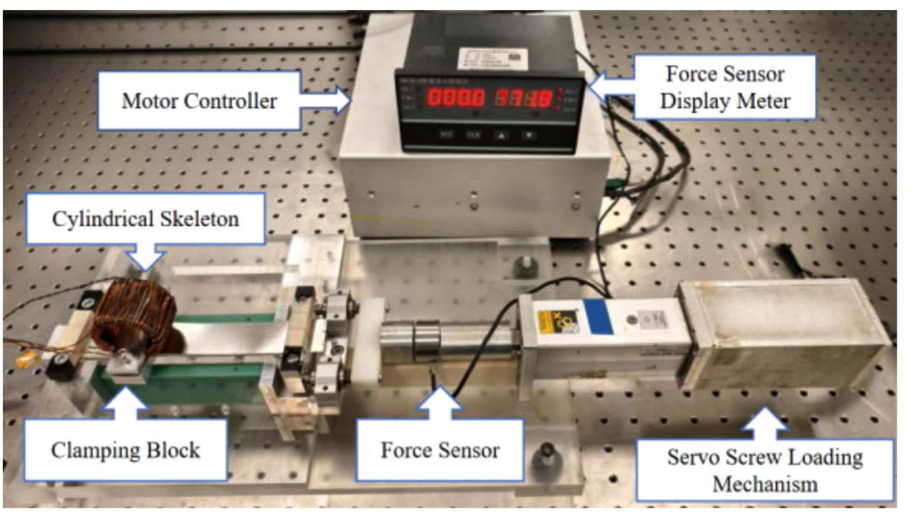
where $V_2(t)$ is the secondary-side voltage, $I(t)$ is the primary-side current, N_1 and N_2 are the number of turns of the excitation winding and the *B*-coil of the sample, respectively, S is the cross-sectional area of the sample, and Le is the average magnetic path length of the sample, which is calculated as follows:

$$Le = 2\pi(r + \frac{d}{2}) \tag{4}$$

The ribbons are wound on a replaceable cylindrical



(a)



(b)

Fig. 1. (Color online) Magnetic property testing system: (a) schematic diagram of the magnetic characteristic testing system, (b) loading device platform.

Table 1. Material characteristics of samples.

Ribbon Model	Length	Width	Thickness	Density	Young's Modulus	Tensile Strength
1K101	260 mm	30 mm	0.026 mm	7.197 g/cm^3	131 GPa	1715 MPa
GT050	260 mm	30 mm	0.05 mm	7.650 g/cm^3	195 GPa	465 MPa

sample frame to form a single-layer closed magnetic circuit, as shown in Fig. 2, so as to avoid magnetic circuit interruption at the ends. The bobbin is made of nylon, a non-magnetic material, and featured replaceable radii (20, 25 and 30 mm) to achieve different curvature conditions. Both ends of the cylinder are connected to a fixed fixture and a tension loading end, respectively; a constant tensile stress is applied and using a servo lead screw mechanism. The servo motor and lead screw loading device ensured stable and controllable tension, and the applied force is monitored in real time and fed back using a force sensor. One end of the amorphous ribbon is fixed to the bobbin base using a clamping block, while the other end is connected to the loading end. To avoid stress concentration at the ends, a soft gasket is attached to the inner surface of the clamping block, ensuring a uniform stress distribution and preventing damage to the ribbon surface. The applied force (F) and tensile stress (σ_t) can be calculated using

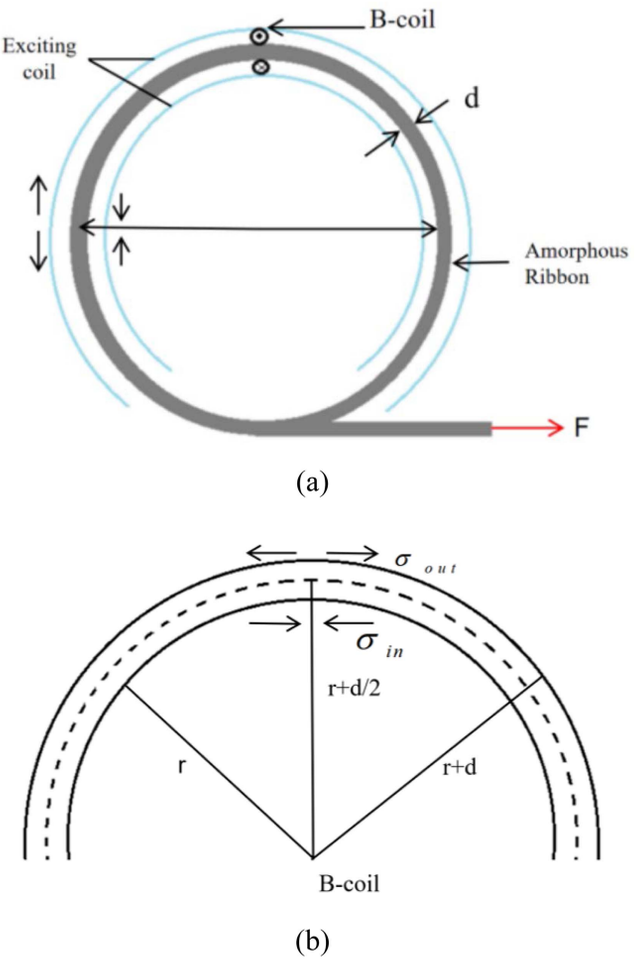


Fig. 2. (Color online) Schematic diagram of the (a) measurement method and (b) schematic bending method.

Eqs. (5) and (6), respectively. The bending stress (σ_b) is determined by the winding radius r of the ribbons and is calculated using Eq. (7).

$$S = wd \tag{5}$$

$$\sigma_t = F / S \tag{6}$$

$$\sigma_b = \frac{Ed}{2r + d} \tag{7}$$

where w is the width of the sample ribbon, d is the thickness of the sample ribbon, E is the Young's modulus of the sample, and r is the radius of the cylindrical bobbin employed. Because r is equal to half of the bobbin diameter D, according to Eqs. (7), a smaller bobbin diameter results in a higher bending stress. For GT050 ultra-thin silicon steel, when E = 195 GPa and d = 0.05 mm, the calculated bending stresses corresponding to the bobbin diameters of 40, 50, and 60 mm are 243.446, 194.805, and 162.365 MPa, respectively. For the 1K101 amorphous ribbon, when E = 131 GPa and d = 0.026 mm, the corresponding bending stresses are 85.095, 68.085, and 56.742 MPa. By replacing cylindrical bobbins, different bending stresses can be applied to the ribbons, thereby enabling the control of the combined bending and tensile stress states.

3. Measurement Results Analysis

To investigate the effect of the bending stress induced by different curvatures on the magnetization behaviours of ultra-thin silicon steel ribbons and amorphous ribbons, measurements are performed using cylindrical bobbins with diameters of 40, 50, and 60 mm without applying tensile stress. All magnetic-property and core-loss results were obtained at a fixed excitation frequency of 50 Hz under sinusoidal magnetic flux-density excitation. According to Eq. (7), the corresponding bending stresses for the GT050 ultra-thin silicon steel ribbons are 243.446, 194.805, and 162.365 MPa, respectively. The corresponding bending stresses for the 1K101 amorphous ribbons are 85.095, 68.085, and 56.742 MPa, respectively. Thus, the bending stress increases as the bobbin diameter and bending radius decrease. To simulate the mechanical stress levels commonly observed in transformer cores (typically below 40 MPa), tensile stresses of 0, 10, 20, 30 and 40 MPa are applied using a servo loading system. All results are averaged over three repeated tests, ensuring a repeatability error of less than 2%.

For the ultra-thin silicon steel ribbons, the hysteresis loops and magnetization curves are recorded under each test condition over a magnetic flux density range of 0.1–1.5 T, with an interval of 0.1 T. For the amorphous alloy ribbons, measurements are carried out over a range of 0.1–1.3 T, with an interval of 0.1 T.

3.1. Ultra-thin silicon steel

Fig. 3 presents the magnetic and loss characteristics of the GT050 ultra-thin silicon steel ribbons without applied tensile stress. As the bending stress increases, the magnetic permeability decreases considerably, while the saturation magnetic flux density decreases slightly. At $\boldsymbol{B}$ = 1.5 T, the hysteresis loops gradually broaden and exhibit a more pronounced S-shaped distortion with increasing bending stress, accompanied by an increase in the coercivity (H_C). Noted that this S-shaped distortion is primarily governed by quasi-static domain wall pinning, induced by the non-uniform bending stress. While higher excitation frequencies will further broaden the loops because of increased eddy current effects, this fundamental stress-induced distortion characteristic remains independent of the frequency.

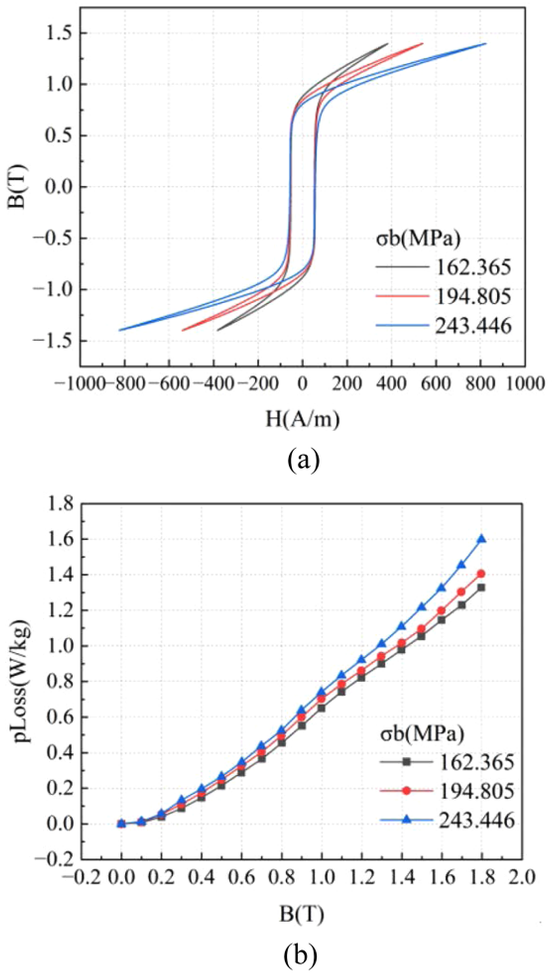


Fig. 3. (Color online) Measurements of ultra-thin silicon steel ribbons under zero applied tensile stress: (a) Hysteresis loops, (b) Core loss.

Specifically, the H_C under a bending stress of 243.446 MPa is 6.27% higher than that under 162.365 MPa. Additionally, the hysteresis loops corresponding to different bending stresses intersect at two symmetric points that are symmetric with respect to the origin. Fig. 3(b) presents the core-loss characteristics under sinusoidal excitation without axial tensile stress. The core loss increases with the bending stress and magnetic flux density. At B = 1.5 T, the core loss at 243.446 MPa is 20.4% higher than that at 162.365 MPa.

Fig. 4 depicts the hysteresis loops at B = 1.5 T under three bending stress levels. For a given bending stress, as the tensile stress gradually increases, the hysteresis loop gradually contracts, accompanied by a decrease in its maximum magnetic field strength and coercivity, and an increase in its remanence. Furthermore, a higher bending stress diminishes the mitigating effect of the tensile stress on coercivity.

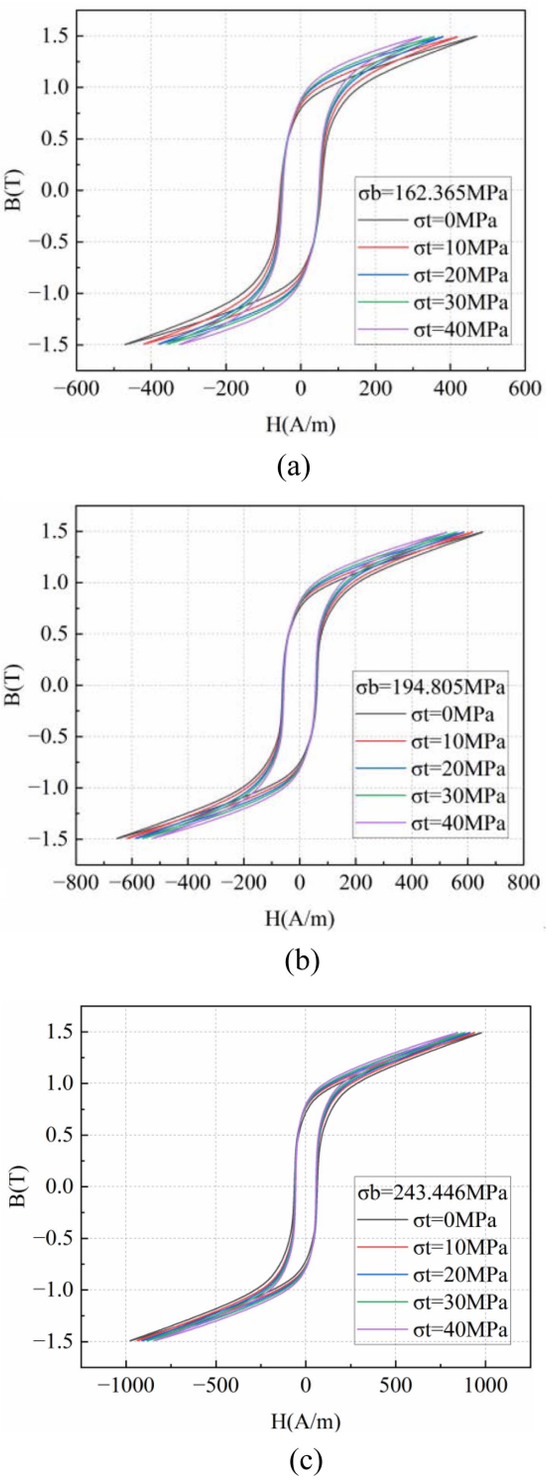


Fig. 4. (Color online) Hysteresis loops of ultra-thin silicon steel ribbons under applied tensile and bending stresses: (a) σ_b = 162.365 MPa, (b) σ_b = 194.805 MPa, (c) σ_b = 243.446 MPa.

Fig. 5 displays the contour maps illustrating the effect of the applied tensile stress on the core loss under bending conditions across various magnetic flux density

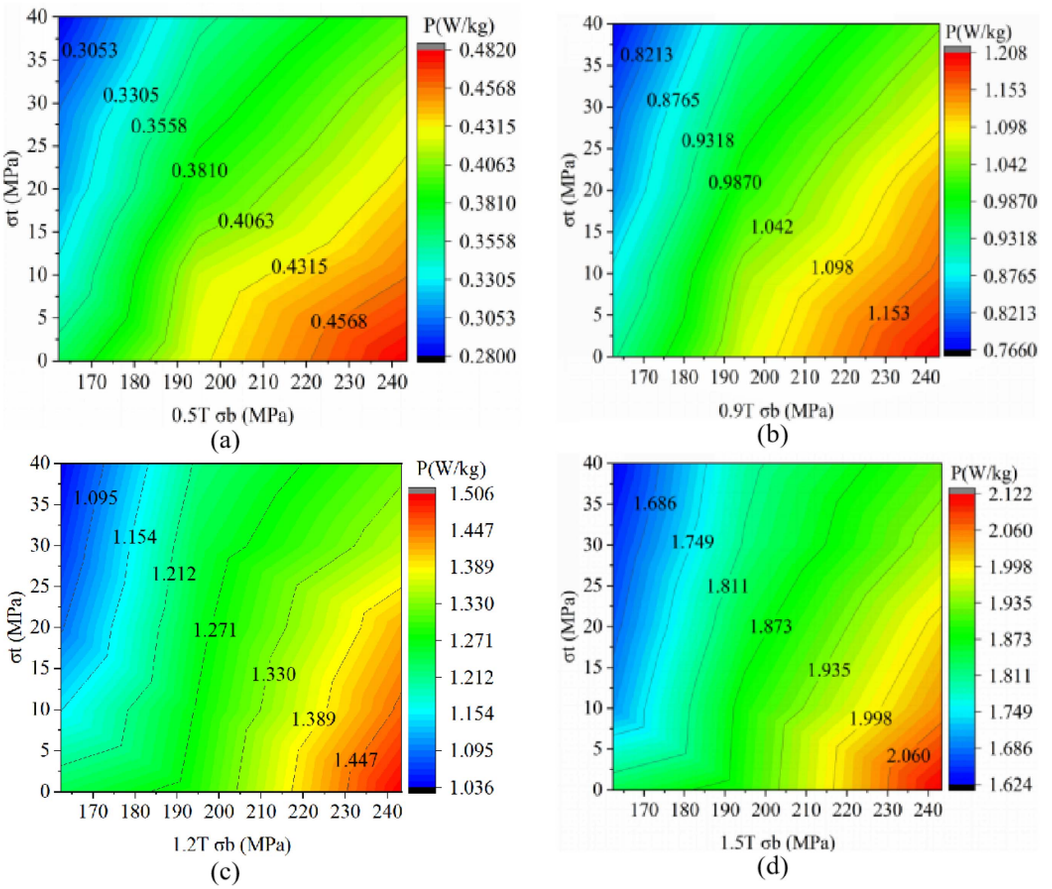


Fig. 5. (Color online) Loss contour maps illustrating the effects of bending stress and tensile stress on ultra-thin silicon steel at different magnetic flux densities: (a) B = 0.5 T, (b) B = 0.9 T, (c) $\boldsymbol{B}$ = 1.2 T, (d) $\boldsymbol{B}$ = 1.5 T.

ranges. The increase in the core loss is nonlinearly related to both bending and tensile stresses. Ultimately, increasing the tensile stress significantly alleviates the loss-enhancing effect induced by the bending stress.

3.2. Amorphous alloy

Fig. 6(a) illustrates the hysteresis loops of the amorphous alloy 1K101 ribbons at B = 1.2 T without the applied tensile stress. Bending stresses of 85.095 MPa, 68.085 MPa, and 56.742 MPa are induced using cylindrical bobbins with diameters of 40, 50, and 60 mm, respectively. As the bending stress increases, the hysteresis loops gradually broaden and shift into an S shape, accompanied by an increase in the coercivity (H_C). Specifically, the H_C under a bending stress of 85.095 MPa is approximately 28.57% higher than that under 56.742 MPa. Additionally, the hysteresis loops corresponding to different bending stresses intersect at two symmetric points about the origin. Fig. 6(b) displays the core loss characteristics under sinusoidal excitation without the axial tensile stress over a magnetic flux density range of 0.1–1.3 T. The core loss increases with bending stress and magnetic flux density, although this upwards trend slows as the flux density approaches 0.7 T. This behaviour indicates that the magnetic properties of the amorphous alloy are more sensitive to the applied stress than those of ultra-thin silicon steel.

Fig. 7 depicts the hysteresis loops at B = 1.2 T under three bending stress levels, with all curves ultimately reaching magnetic saturation. For a given bending stress, as the axial tensile stress gradually increases, the hysteresis loop gradually contracts, accompanied by a decrease in its H_C. Furthermore, a higher bending stress diminishes the mitigating effect of the tensile stress on coercivity. Specifically, at a bending stress of 56.742 MPa, the H_C under 40 MPa tensile stress is 11.9% lower than that without tensile stress (0 MPa). However, when the bending stress increases to 85.095 MPa, the H_C under a 40 MPa tensile stress decreases by only 3% relative to that under 0 MPa .

Fig. 8 displays the contour maps illustrating the effect of the applied tensile stress on the core loss under

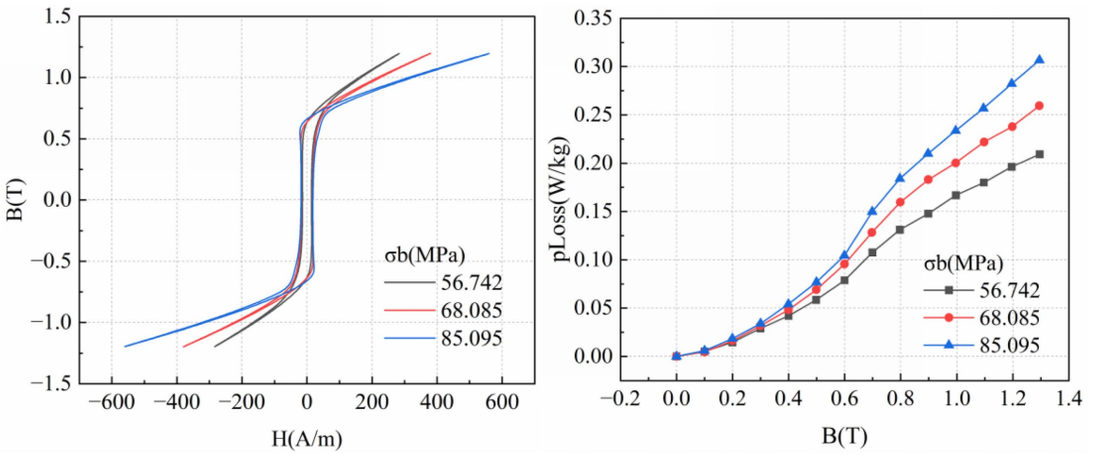


Fig. 6. (Color online) Measurements of amorphous ribbons under zero applied tensile stress: Hysteresis loops, (b) Core loss.

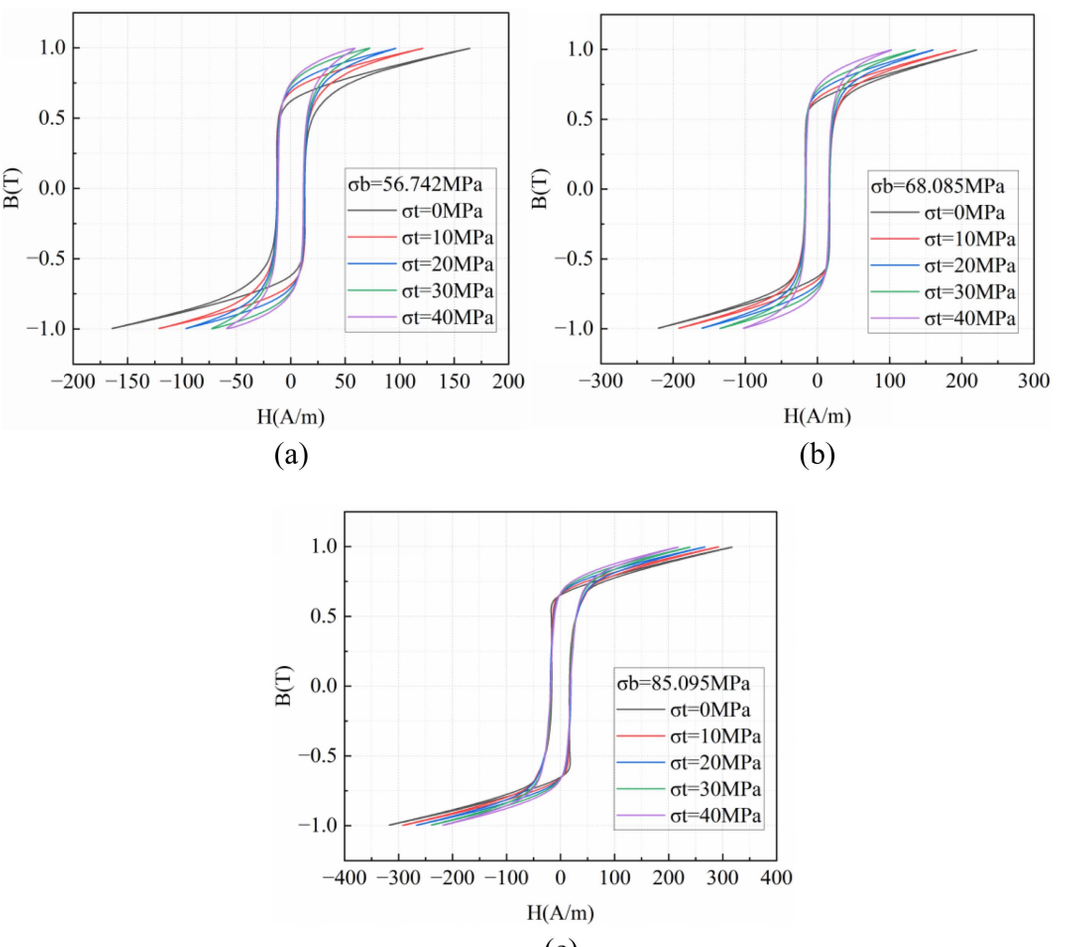


Fig. 7. (Color online) Hysteresis loops of amorphous ribbons under the combined action of applied tensile and bending stresses: (a) σ_b = 56.742 MPa, (b) σ_b = 68.085 MPa, (c) σ_b = 85.095 MPa.

bending conditions across a magnetic flux density range of 0.3 T to 1.3 T. At a given magnetic flux density, the core loss increases significantly with increasing bending stress, although the rate of this increase gradually slows.

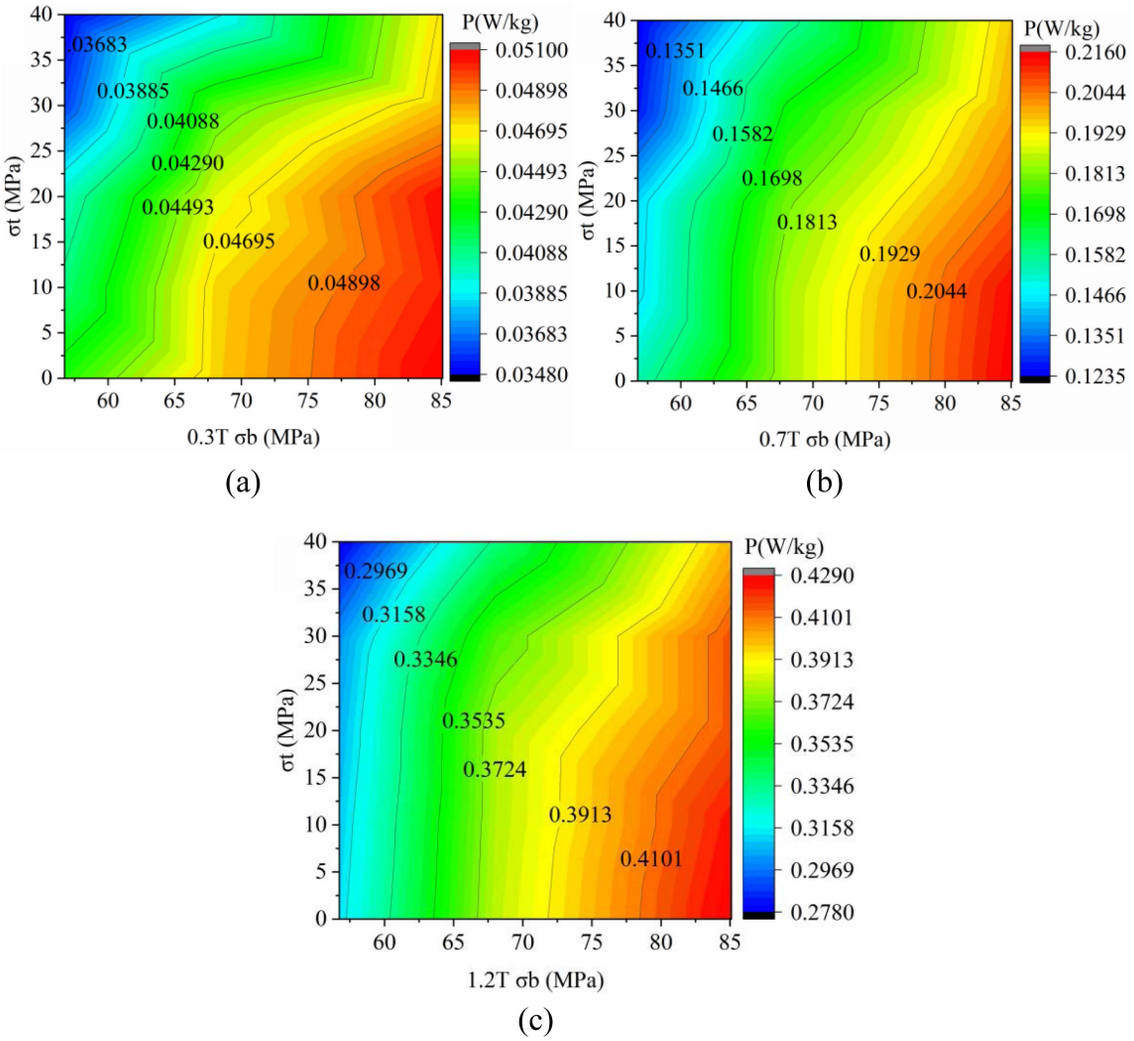


Fig. 8. (Color online) Loss contour maps illustrating the effects of bending stress and tensile stress on amorphous ribbons at different magnetic flux densities: (a) B = 0.3 T, (b) B = 0.7 T, (c) B = 1.2 T.

Conversely, for a given bending stress, the core loss decreases as the axial tensile stress increases. The variation in the core loss is nonlinearly related to both bending and tensile stresses. Additionally, the gradient of the contour lines for the amorphous ribbons is steeper than that observed for the ultra-thin silicon steel. This finding indicates that the sensitivity of the amorphous alloy's core loss is further enhanced with increasing stress.

Compared with the GT050 ultra-thin silicon steel, the 1K101 amorphous ribbon exhibits larger relative changes in the coercivity and core loss under mechanical stress. This difference can be explained by the magnetostriction characteristics and magnetoelastic anisotropy of the two materials. The magnetoelastic anisotropy induced by mechanical loading is proportional to the product of the saturation magnetostriction coefficient and the applied stress. The 1K101 Fe-based amorphous alloy has positive and appreciable magnetostriction, while its amorphous structure has weak magnetocrystalline anisotropy. Consequently, external stress can readily modify its effective magnetic anisotropy, domain configuration, and domain-wall motion [14]. In particular, axial tensile stress favours domain alignment along the loading direction, while the tensile–compressive stress distribution produced by bending introduces non-uniform magnetoelastic anisotropy across the ribbon thickness.

By contrast, the pronounced Goss texture of the GT050 grain-oriented silicon steel aligns its easy magnetization axes close to the rolling and magnetization directions. Its longitudinal magnetostriction along the rolling direction is relatively low, and its domain configuration is therefore less strongly perturbed by the additional stress-induced anisotropy [15]. These different magnetoelastic characteristics explain why the 1K101 ribbon exhibits greater

stress-induced changes in the coercivity and core loss under the present experimental conditions.

4. Conclusion

This paper establishes a magnetic property measurement system considering both bending stress and tensile stress. The experimental results indicate that at an excitation frequency of 50 Hz, applied bending stress alters the magnetic properties of ultra-thin silicon steel and amorphous alloy ribbons, resulting in magnetic degradation, while tensile stress can mitigate this effect. Notably, amorphous alloy ribbons are more significantly affected by both bending and tensile stresses. This study provides valuable insights into the optimal design of electrical machines and toroidal core transformers, as well as the ribbon winding process during manufacturing.

Acknowledgment

This work was supported by the National Natural Science Foundation of China under Grant No. 52130710 and 52407005 and supported by Hubei Provincial Engineering Technology Research Center for Power Transmission Line, China Three Gorges University, Grant No. 2024KXL04 and by the Natural Science Foundation of Hebei Province under Grant No. E2026202076.

References

[1] A. Najafi and I. Iskender, Electr. Eng. **100**, 1125 (2018).
[2] Z. Li, Y. Ma, A. Hu, L. Zeng, S. Xu, and R. Pei, Materials **15**, 8522 (2022).
[3] Y. Dou, Y. Li, C. Zhang, S. Yue, and J. Zhu, IEEE Trans. Magn. **56**, 7512004 (2020).
[4] Y. Maeda, S. Urata, H. Nakai, Y. Takeuchi, K. Yun, S. Yanase, and Y. Okazaki, AIP Adv. **7**, 056664 (2017).
[5] A. Daem, P. Sergeant, L. Dupré, S. Chaudhuri, V. Bliznuk, and L. Kestens, Materials **13**, 4361 (2020).
[6] P. Rękas, M. Nowicki, P. Gazda, T. Charubin, T. Szumiata, and R. Szewczyk, J. Magn. Magn. Mater. **577**, 170791 (2023).
[7] L. Chen, D. Yan, T. Ben, L. Jing, and Q. Liu, AIP Adv. **13**, 025340 (2023).
[8] L. Chen, X. Liu, T. Ben, D. Yan, and X. Zhang, AIP Adv. **14**, 025112 (2024).
[9] T. Mizuta, Y. Tani, and K. Fujiwara, IEEE Trans. Magn. **54**, 6001005 (2018).
[10] X. Zhu, Y. Li, Y. Dou, and J. Gao, AIP Adv. **14**, 015150 (2024).
[11] J. Li, S. Yue, Y. Dou, J. Zhou, and Y. Li, AIP Adv. **15**, 035119 (2025).
[12] T. Sato and T. Todaka, IEEE Trans. Magn. **54**, 2002904 (2018).
[13] Y. Chang, C. Hsu, H. Chu, and C. Tseng, IEEE Trans. Magn. **47**, 2780 (2011).
[14] W. Zheng, G. Zhang, Q. Zhang, H. Yu, Z. Li, S. Song, M. Gu, S. Zhou, and X. Qu, Metals **13**, 1823 (2023).
[15] X. Zhao, Y. Du, Y. Liu, Z. Du, D. Yuan, and L. Liu, Materials **12**, 2156 (2019).